IEEE Access
Multidisciplinary | Rapid Review | Open Access Journal

Received November 13, 2017, accepted March 4, 2018, date of publication March 15, 2018, date of current version April 18, 2018.

Digital Object Identifier 10.1109/ACCESS.2018.2816466

Multiview mm-Wave Imaging With Augmented Depth Camera Information

JAIME LAVIADA[1], MIGUEL LÓPEZ-PORTUGUÉS[1], ANA ARBOLEYA-ARBOLEYA[2], AND FERNANDO LAS-HERAS[1], (Senior Member, IEEE)

[1]Department Ingeniería Eléctrica, Universidad de Oviedo, 33203 Gijón, Spain
[2]Universidad Rey Juan Carlos, 28942 Madrid, Spain

Corresponding author: Jaime Laviada (jlaviada@tsc.uniovi.es)

This work was supported in part by Ayudas Fundación BBVA a Investigadores y Creadores Culturales 2016, in part by the Ministerio de Ciencia e Innovación of Spain /FEDER under Project TEC2014-55290-JIN and Project TEC2014-54005-P, and in part by the Gobierno del Principado de Asturias (PCTI)/FEDER-FSE under Project GRUPIN14-114.

ABSTRACT This paper introduces a hybrid method that combines two 3-D imaging methods of very different nature but complementary. On the one hand, a depth camera, also known as RGB-D camera, is used in order to obtain a 3-D scan of the target under test. On the other hand, a synthetic aperture radar at millimeter-wave frequency band is used to exploit the penetration capabilities of these waves, allowing electromagnetic imaging. As a result, the system can provide two complementary and aligned 3-D models. In contrast to the previous work, in which the position estimation and the external 3-D model relied on conventional optical cameras, this setup can construct the model even in the case of flat textures as it does not resort to color information at any stage. Several examples, in which the millimeter-wave scanner is validated by raster scan, are presented for people screening revealing the validity of the approach.

INDEX TERMS Millimeter-wave imaging, portable camera, multiview imaging, depth camera, structured light, synthetic aperture radar.

I. INTRODUCTION

Object and people scanning is a well-known tool that enables to build a computational three-dimensional (3D) model of a given target. On the one hand, the most widespread approach is based on scanning an object so that a model of its visible layer, which is the most *external layer*, is calculated. This goal can be achieved by means of multiple technologies such as lasers [1] or a collection of images taken from optical cameras [2], [3]. Also, depth cameras, which will be later introduced, can be used for this purpose.

Depending on the technology and investment, different degrees of accuracy and scanning speed can be achieved. It is also relevant to observe that these approaches usually entail a relatively low computational burden. Furthermore, it has been demonstrated that currently smartphones are capable to perform real-time 3D external reconstruction from the information captured by their built-in cameras [4].

On the other hand, the use of other technologies such as X-ray computed tomography, microwaves [5], [6] and millimeter-waves (mm-waves) [7], [8] can provide information of not only the visible (i.e., external) surface but also about the *inner layers*. However, this advantage entails diverse expenses such as the use of ionizing radiation (X-rays) or the lost of resolution with respect to conventional optical cameras (micro- and mm-waves).

In the last years, the use of *mm-wave technology* has widespread for different reasons. First, this frequency band provides very interesting balance between penetration capabilities and resolution. Consequently, it is appealing for applications such as people screening [7], [9], [10] or automotive radars [11]. Second, this frequency band can also provide very high absolute bandwidth when compared to standard microwave communications, which has motivated its use for high data-rate wireless communications [12]–[14].

In addition, micro- and mm-wave camera and portable systems are progressively being developed [6], [15], [16]. This fact has motivated the use of mm-wave cameras as portable 3D electromagnetic scanners [17] in a similar fashion to the aforementioned smartphones scanners with capability to build 3D models on-the-fly [4]. In this framework, [17] proposed the use of a Synthetic Aperture Radar (SAR) to scan a certain object or body at mm-wave frequencies by combining multiview information. The data were collected from multiple angles in order to achieve a complete model scan.

The position and attitude of the scanner at each view acquisition were estimated by using an optical camera. Thus, by taking pictures at the same positions as the mm-wave acquisitions are performed and processing them with Structure from Motion techniques [18], the scanner rotation angles and positions can be found to apply the appropriate multiview merge algorithms. The possibility of reducing the number of transmitting and receiving elements resorting to multistatic techniques was later studied in [19].

Nevertheless, as pointed out in [17], this positioning scheme requires to find a number of common key points from different views so that the position can be calculated by triangulation. In particular, the scale-invariant feature transform (SIFT) was used to compute the key points in [17]. Consequently, the technique is expected to fail when considered objects lack of textures.

In order to bypass the previous limitation, the use of *depth cameras*, also known as RGB-D cameras [20], [21], is proposed in this paper. These cameras are based on two different approaches. The first one is usually known as *structured light* and it relies on projecting a known set of (infrared) patterns into the object so that its shape can be estimated from the deformed pattern [22]. The second technique is usually known as *time-of-flight* and it is based on measuring how long it takes for light to travel the round trip from the sensor to a given scene point [23]. It is worthy to note that these tools have also been hybridized with mm-wave imaging for people screening with booth-size flat-panels to help reducing the observation volume [24].

The main contribution of this paper is the extension of the mm-wave portable scanner concept presented in [17] by replacing the conventional optical camera with a depth camera. Thus, positioning is not accomplished by finding key points but by comparing point clouds (PCs) acquired by the depth camera. This change does not affect the ability of the system to produce a double model including the external and inner layers. The accuracy achieved by this combination is assessed for several cases in the *people screening* context.

This paper is structured as follows. First, an overview of the approach combining mm-wave and depth camera information is presented. Next, the details of both imaging systems are detailed. After that, the merging approach to create the double model strategy is presented. In the Results section, the accuracy and time to estimate the position with the depth camera are evaluated and, next, several examples considering one dimensional as well as two-dimensional synthetic apertures are shown. Finally, the conclusions are drawn.

II. mm-WAVE SCANNER ENHANCED BY DEPTH CAMERA INFORMATION

A. GLOBAL OVERVIEW

The scanner proposed in [17] is based on a relatively small aperture (e.g., a maximum size of 15 cm was considered in [17]) so that it can be moved around the object under test to perform a multiview scan.

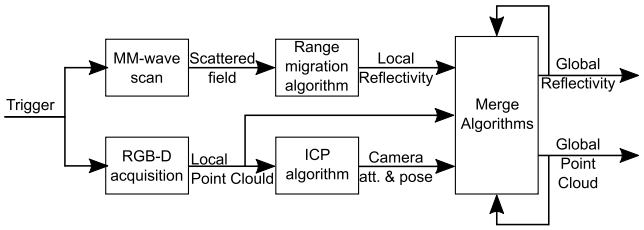

Fig. 1. Diagram of the steps of the proposed scanning involving electromagnetic and depth camera information.

Fig. 1 depicts a diagram with the different steps of the scanning process. As shown, a mm-wave acquisition by means of multiple transmitters and receivers is performed in parallel to the acquisition of a depth camera. On one hand, the acquired scattered field is processed by means of standard range-migration techniques [25] to obtain the reflectivity evaluated on a regular grid of points. On the other hand, the PC measured by the depth camera is processed by means of the iterative closest point (ICP) algorithm [26] to find out the movement with respect to the previously acquired PC, i.e., to know the relative movement between two depth camera acquisitions. Consequently, the global camera attitude and position can be estimated by taking into account the cumulative movements and rotations.

Finally, the reflectivity and PC data are merged with the data from previous acquisitions yielding a double 3D model that contains two sets of information. One related to the external layer of the object (global point cloud) and the second one related to inner layers (global reflectivity).

B. mm-WAVE IMAGING

In this work, a regular grid of monostatic transceivers is considered as in [7] and [17]. Consequently, standard range-migration imaging algorithms are used. In particular, the approach described in [25], which relies on fast Fourier transforms, is employed. Thus, if a system of coordinates, local to the scanner, is defined as (x', y', z'), where the scanner aperture is assumed to be along the plane $y' = 0$, then the reflectivity $\rho(x', y', z')$ can be computed as:

$$\rho(x', y', z') = \mathcal{F}_k^{-1}\left\{\mathcal{F}_{xz}\left\{s(x', z', \omega)\right\} \times \exp\left(-j\sqrt{4k^2 - k_x^2 - k_z^2}D\right)\right\} \quad (1)$$

where $s(x', z', \omega)$ is the acquired complex amplitude for the transceiver placed at the aperture position (x', z') when it is transmitting a tone at the angular frequency ω; D is the distance along the y axis from the center of the scanner aperture to the center of the observation grid; $\mathcal{F}_{xz}\{\cdot\}$ denotes a bidimensional Fourier transform from the (x', z') space to the (k_x, k_z) space; $k = \omega/c$ is the wavenumber, being c the speed of light; $\mathcal{F}_k\{\cdot\}$ denotes a 3D Fourier transform from the k-domain defined by the coordinates (k_y, k_y, k_z), which satisfy the condition with $k^2 = k_x^2 + k_y^2 + k_z^2$, to the spatial

domain defined by the Cartesian coordinates (x', y', z'). This three-dimensional reflectivity data, after processing, can be presented as an image [7], [9], [17].

C. DEPTH CAMERA POSITIONING

The positioning relies on the information provided by a depth camera, which is based on *structured light*. In order to generate a depth frame, an infrared projector illuminates the object under test with a set of predefined patterns. These patterns are warped by the object surface, reflected back to the camera, and then captured by the infrared sensor. The infrared pixels are processed and combined with the RGB sensor data to generate a PC with color information.

In this work, the Iterative Closest Point algorithm (ICP) implementation from the Point Cloud Library (PCL) [27], which is based on a *point-to-plane* strategy, is employed. The 3D model generation and camera positioning procedure may be divided in three steps: i) *acquisition* of a new PC, ii) *registration* of the current PC (i.e., calculation of the translation and rotation matrix for the new PC) and iii) *integration* of the new vertices into the model. From the transformation matrix that is obtained for each PC, the relative camera position (i.e., translation and rotation from the previous position) can be calculated.

Since a classical ICP implementation has been used, new points are integrated into the model step by step. Therefore, error accumulation may occur, thus hindering a perfect match of the borders when scanning closed surfaces. In order to overcome the above-mentioned *loop closure* problem, global ICP variants could be used [28]–[30].

D. MODEL MERGE

Once the position and attitude of the scanner is known, it is possible to translate the local system of coordinates into a global one so that the last acquired data can be merged with the data acquired in previous acquisitions. This stage can be done for both datasets: mm-wave image and PC. In the case of the reflectivity, the technique proposed in [17] is used. Thus, the reflectivity at the m-th acquisition ρ_m can be merged with the global reflectivity as:

$$\Gamma_m(\vec{r}) = \max\{|\Gamma_{m-1}(\vec{r})|, |\rho_m(\vec{r})|\}, \tag{2}$$

where Γ_m denotes the global reflectivity after the m-th acquisition which is evaluated at the point $\vec{r}$, which is expressed in a global coordinates system. Thus, it is relevant to observe that the reflectivity $\rho_m(\vec{r}')$ must be translated into the global system of coordinates before the merge operation. Since the rotation and translation matrices characterizing the movement between consecutive positions are obtained during the ICP application, the translation from the local coordinates systems to the global one can be easily performed by concatenating these translations and rotation operations. As discussed in [17], this incoherent combination described in (2) is preferred versus other coherent combination approaches since the scanner position is not expected to be known with accuracy equal or better than the operating wavelength, as required for coherent combination [31].

In order to build a general 3D model from the different registered PC, the PCL library tools are used [27]. Thus, the integration step is performed as follows: i) an initial model mesh is reconstructed from the PC, which is registered with the first camera position, ii) the following registered PCs —each one from a different camera position— are subsequently merged with the model one by one. Merging is done by searching for the nearest neighbors from the PC to the current model mesh. On the one hand, if the angle between the normal vectors at a new and an old point is smaller than a given threshold both points are considered to be the same one. On the other hand, if the distance between them is higher than a given threshold those points are added to the mesh as new vertices. Finally, the outlier rejection is based on *visibility confidence* and *maximum age*. The former is the number of unique directions from which a vertex has been recorded, whereas the latter is amount of time since a vertex has been recorded for the last time. If a vertex exceeds the maximum age without reaching a minimum visibility confidence, then it is removed from the mesh.

III. RESULTS

In order to illustrate the performance of the method, several examples for concealed weapon detection are considered. In contrast to [17], textureless clothing is employed. In particular, a white T-shirt has been used to cover a mannequin with different kind of attached (and hidden) threatens. The mannequin is covered by aluminum foil to increase its reflectivity as used in similar studies using also aluminum foil [32] or conductive paint [24].

In this proof of concept, instead of considering a fully electronic scan as the one for a final device such as in Fig. 1, a raster scan with a general purpose single element has been considered. Although this kind of scan is inherently much slower than a fully electronic device (e.g., [16]), it is still representative of the quality that could be achieved by the scanner.

The measurement setup is implemented by means of linear multi-axis and rotary positioners, as schematically shown in Fig. 2, in the measurement range described in [33]. The final device is supposed to acquire the field at several positions around the target, as described by the blue dashed line (Fig. 2). In order to do that, the two-dimensional aperture of the scanner is synthesized by the linear multi-axis positioner, while the circular displacement is achieved by rotating the target, installed on top of the rotary positioner.

After synthesizing each aperture, the depth camera was moved to the center of the aperture for the sake of simplicity. In a real device, this camera could be installed on an edge of the aperture, in that case the corresponding offset should be corrected to align both 3D models. Although roll and pitch changes of the scanner cannot be considered in this setup, the corresponding values of these angles are estimated from the depth camera information and are reported.

TABLE 1. Real and estimated camera positions for the one-dimensional aperture example. In addition, the attitude described by yaw (γ), pitch (α) and roll (β) is also given. Estimated positions and attitudes from the depth camera information are denoted by $\hat{\cdot}$.

Camera position						Camera attitude					
x [cm]	$\hat{x}$ [cm]	y [cm]	$\hat{y}$ [cm]	z [cm]	$\hat{z}$ [cm]	γ [deg.]	$\hat{\gamma}$ [deg.]	α [deg.]	$\hat{\alpha}$ [deg.]	β [deg.]	$\hat{\beta}$ [deg.]
29.88	31.04	17.25	17.71	0	0.12	-60	-59.69	0	-1.47	0	2.57
22.18	22.78	26.43	26.93	0	0.32	-40	-39.49	0	-1.37	0	1.22
11.80	11.94	32.42	32.74	0	0.2	-20	-19.56	0	-0.76	0	0.03
0	0	34.50	34.50	0	0	0	0	0	0	0	0
-11.80	-11.78	32.42	32.20	0	0.24	20	19.35	0	0.73	0	-0.56
-22.18	-22.45	26.43	25.81	0	0.82	40	39.55	0	1.80	0	-0.14
-29.88	-30.19	17.25	16.30	0	1.24	60	59.42	0	2.45	0	0.56

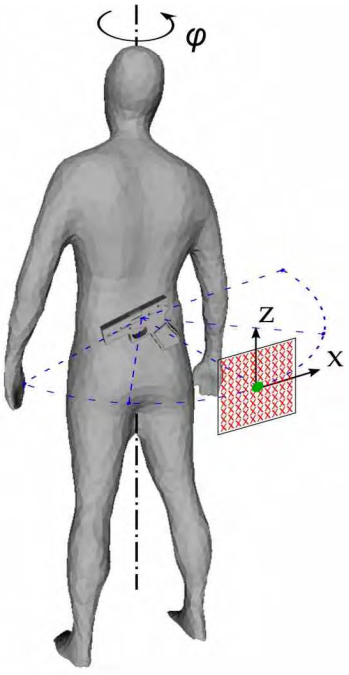

Fig. 2. Measurement setup to mimic the portable scanner.

Several scanner trajectories have been considered and analyzed with open source software [34] employed in [17]. As it could be expected, the software was not able to find a common model merging all the views due to the lack of keypoints when textureless clothing is analyzed. For this reason, only results regarding the depth camera positioning are reported here.

An Intel® RealSense™ SR300 depth camera (short-range optimized) is attached to the general purpose mm-wave module. The camera uses coded light depth technology and operates at VGA resolution (640 × 480 pixels). In addition, a bounding box of 34 × 55 × 32 cm is set in order to filter out any external object that could affect the positioning accuracy. The minimum required overlap between two consecutive PCs is set to 70% to guarantee the proper functioning of the ICP algorithm. Moreover, the execution time associated to the registration and integration steps has been reduced by limiting the maximum allowed angle between normal vectors of corresponding points in two consecutive PCs to 10°. In addition, several intermediate positions have also been considered, and reported for each example, to increase the overlap between two consecutive acquisitions.

The workstation used to perform the computational tasks shown in this section consists of 2× Intel Xeon E5-2650v3 CPUs (2.3–3.0 GHz clock rate) and 256 GB of RAM. However, the code was forced to run using single-threading. In addition, reflectivity computational times are only reported for two-dimensional examples, as they are the most representative ones.

A. ONE-DIMENSIONAL APERTURE SCANNER EXAMPLE

In this example, a one-dimensional aperture of 115 transmitters equally spaced by 1.4 mm along the x' axis is considered. In contrast to standard mm-wave scanners, whose bandwidth typically ranges from a 5% to a 10%, the entire W band (75 GHz-110 GHz) is considered in order to have a good range resolution to detect artifacts introduced by the depth camera positioning.

The object under test is composed by a mannequin with an attached metallic bar whose thickness is 2 cm (see Fig. 3).

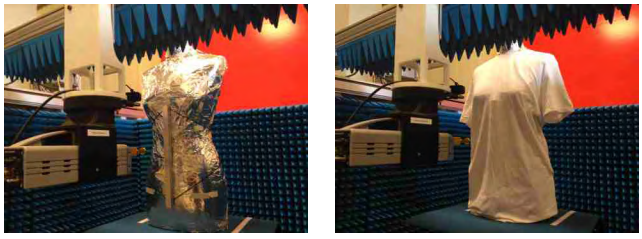

(a) (b)

Fig. 3. Setup for the one-dimensional aperture scanner: a) without clothing; b) with clothing.

The object was scanned from seven different positions (and the corresponding attitudes) whose absolute coordinates (and the corresponding angles) are known, since positioning is made by means of an accurate multiaxis-positioner. Those positions and attitudes will be used as references in order to compute the error between the estimated position and attitude, obtained from the ICP algorithm, and those references. Both reference and estimated positions for the microwave camera are shown in Table 1, together with the angles defining the attitude of the camera. In order to compare

the real and estimated positions, the position and rotation matrix corresponding to the central position (i.e., the fourth one) have been defined to be the same as the real position. In this example, the relative error between two consecutive positions ranges from 0.3 mm to 2.6 mm, with a mean value of 1.1 mm. Moreover, the absolute error for the whole scanning path is 1.7 cm. The time spent in the registration step ranges from 0.5 s to 0.7 s, whereas the time required by the integration step is 0.2 s.

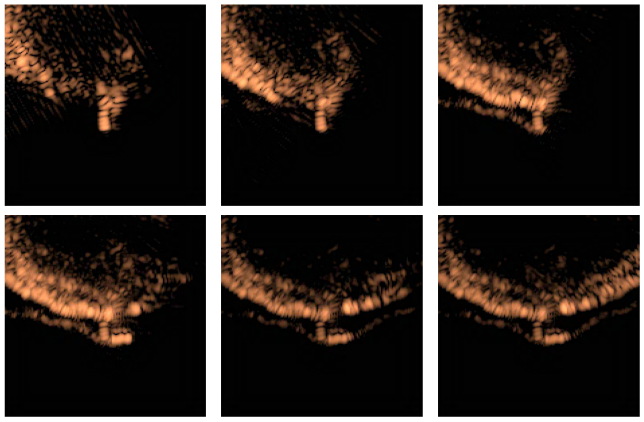

Fig. 4. Partial cumulative reflectivity results with depth camera positioning for the one-dimensional aperture scanner moved around a mannequin with an attached bar. Positions from 1 to 6, ordered as shown in Table 1 are shown starting from upper left corner.

The cumulative reconstructed reflectivity for the first six scanner positions is shown in Fig. 4 revealing that the different overlapped acquisitions can be merged without visible artifacts. In order to further validate the approach, the final reflectivity after the seven positions is shown for the case of the real and estimated positions in Fig. 5 with a very good agreement between both of them.

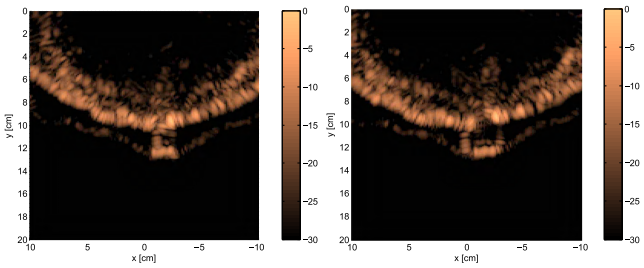

(a) (b)

Fig. 5. Computed reflectivity for the one-dimensional aperture scanner example with: a) real positions; b) positions estimated from depth camera information.

Fig. 6 shows an overlay of the computed reflectivity after merging the multiple local reflectivities and the global PC computed by integrating the different depth camera acquisitions. An in-depth inspection of this figure reveals that the protrusion in the reflectivity matches well the deformation in the clothing.

It is worth noting that some points of the PC are shown in black color in Fig. 6. Due to the architecture of the used depth camera, which maps the RGB information from a standard

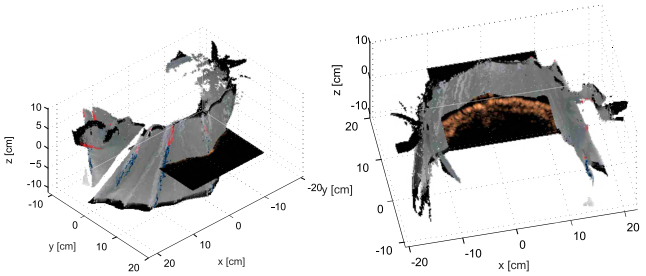

Fig. 6. Computed reflectivity for the one-dimensional scanner aperture example with the overlayed PC obtained by integrating multiple views of the depth camera. Two different points of view are reported.

camera into the points acquired by the depth camera sensor (with a different *principal point* from the RGB one), some points in the PC can have depth information but not color information. These points, which are mostly located on the borders, have *reliable* depth information and, therefore, they can be used safely in the position estimation. In the global point cloud shown in Fig. 6, , these points are black colored.

B. TWO-DIMENSIONAL SCANNER APERTURE EXAMPLES

In this example, a two-dimensional aperture is considered to provide full 3D imaging capabilities. In this case, the modeled scanner aperture comprises 115 × 115 transceivers with the same spacing as in the previous example, i.e., 1.4 mm. The frequency range is reduced to 114 points ranging from 95.04 GHz to 104.93 GHz (i.e., a frequency bandwidth of approximately 10%).

In this case, a replica gun is attached to the mannequin as shown in Fig. 7.

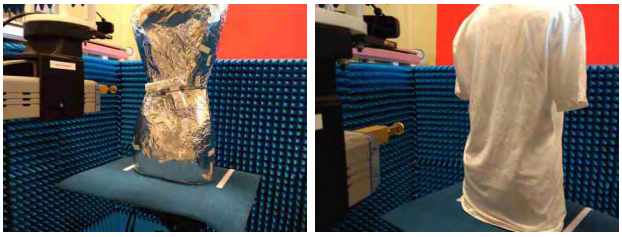

(a) (b)

Fig. 7. Imaging of a mannequin with an attached gun: a) without clothing; b) with clothing.

The setup is performed by combining rotations of the mannequin together with movements of the center of the scanner aperture in order to provide an arbitrary, though realistic, trajectory. In this example, nine different points of view are considered. In particular, the equivalent positions shown in Table 2 are used. The relative error between two consecutive positions ranges from 1.2 mm to 4.1 mm, with a mean value of 2.4 mm. Furthermore, the absolute error for the entire scanning path is 2.2 cm. While the time measured for the registration step ranges from 0.8 s to 1.2 s, the time required by the integration step is 0.2 s.

Partial results obtained for the nine positions of this example are depicted in Fig. 8, showing that the profile behind

TABLE 2. Real and estimated camera positions for the gun example. In addition, the attitude described by yaw (γ), pitch (α) and roll (β) is also given. Estimated positions and attitudes from the depth camera information are denoted by $\hat{\cdot}$.

Camera position						Camera attitude					
x [cm]	$\hat{x}$ [cm]	y [cm]	$\hat{y}$ [cm]	z [cm]	$\hat{z}$ [cm]	γ [deg.]	$\hat{\gamma}$ [deg.]	α [deg.]	$\hat{\alpha}$ [deg.]	β [deg.]	$\hat{\beta}$ [deg.]
26.53	27.94	24.61	24.5	1.5	2.2	-36	-37.10	0	-2.55	0	0.85
20.43	21.36	28.67	28.63	2.5	3.2	-24	-24.60	0	-2.44	0	0.26
14.02	14.70	32.29	32.24	2.5	3.31	-12	-12.57	0	-2.30	0	-0.30
3	3.24	32.5	32.36	2.5	2.68	0	-0.33	0	-0.97	0	-0.51
0	0	34.5	34.5	0	0	0	0	0	0	0	0
-6	-5.63	33.5	33.34	1.5	0.9	0	-0.78	0	1.79	0	0.39
-14.02	-13.58	32.29	32.01	3.5	2.87	12	10.66	0	2.38	0	0.35
-20.43	-20.13	28.67	28.27	3.5	2.79	24	22.51	0	2.60	0	0.30
-26.53	-26.56	24.61	23.96	2.5	1.66	36	34.93	0	2.78	0	0.42

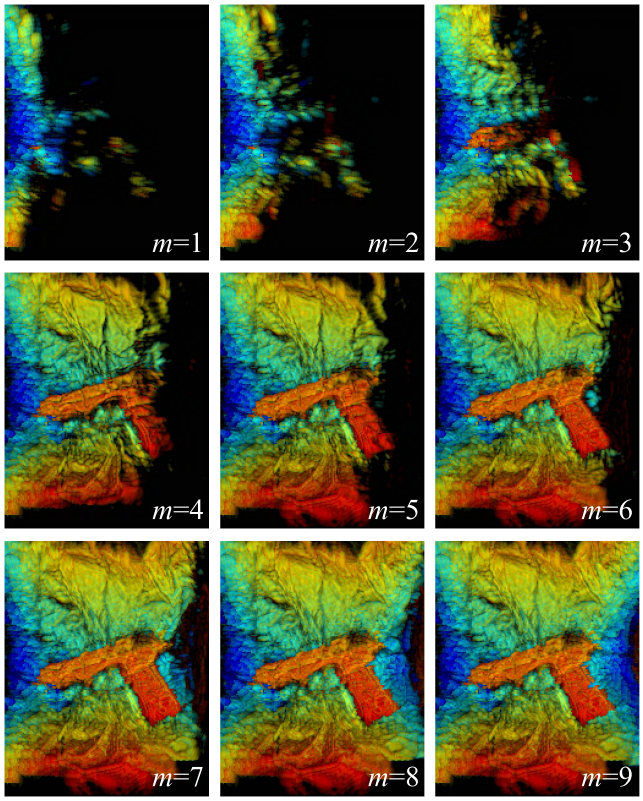

Fig. 8. Partial results for the handgun scanned with a two-dimensional aperture corresponding to the global reflectivity Γ_m for $m = 1, 2, \ldots, 9$ (*left-to-right* then *top-to-bottom*) depicted using the color scheme proportional to the maximum depth and reflectivity amplitude.

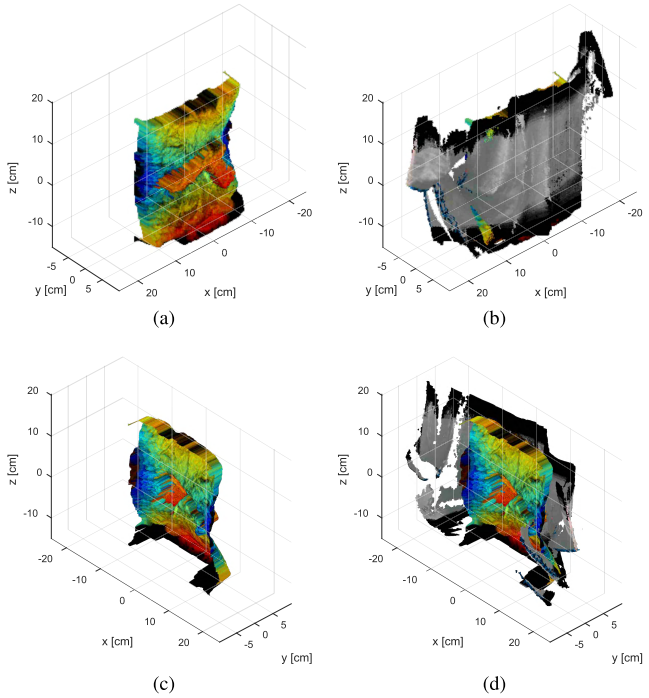

Fig. 9. Imaging of a mannequin with an attached gun: a) front view of the mm-wave model; b) front view of the mm-wave model with the integrated PC; c) rear view of the mm-wave model; d) rear view of the mm-wave model with the integrated PC.

the clothing, including the concealed weapon, is perfectly imaged. Computational time for each partial reflectivity ranges from 1.17 s to 1.25 s. After computing these reflectivities, they are merged with the previous ones into a regular grid of 168 × 140 × 210 points with 1.4 mm spacing. In Fig. 8, the colors at each 2D position (x_0, z_0) are assigned proportional to the position of the maximum of the function $g(y) = \Gamma_m(x_0, y, z_0)$, i..e, proportional to $y_0 = \arg\max_y g(y)$. In addition, the brightness of the color in Fig. 8 is weighted by the amplitude of the reflectivity at the corresponding point $|\Gamma_m(x_0, y_0, z_0)|$ [17].

As in the previous example, the overlay between the 3D mm-wave model and the one obtained by integrating the PCs from the depth camera (i.e., the global PC) is shown Fig. 9 with an excellent agreement between both models. The 3D mm-wave model has been represented by calculating a surface $w(x, z) = \arg\max_y \Gamma_m(x, y, z)$. The same color scheme as in Fig. 8 has been used.

Next, an example with the same parameters as in the previous example is considered. However, a pair of scissors are attached to the mannequin torso as shown in Fig. 10 and the positions given in Table 3 are used. In this application example, the relative error between two consecutive positions ranges from 0.9 mm to 7.5 mm, with a mean value of 3.2 mm. In addition, the absolute error for the whole path is 2.4 cm. The time required by the registration ranges from 0.9 s to 1.3 s, whereas the time for the integration is 0.2 s.

TABLE 3. Real and estimated camera positions for the scissors example. In addition, the attitude described by yaw (γ), pitch (α) and roll (β) is also given. Estimated positions and attitudes from the depth camera information are denoted by $\hat{\cdot}$.

Camera position						Camera attitude					
x [cm]	$\hat{x}$ [cm]	y [cm]	$\hat{y}$ [cm]	z [cm]	$\hat{z}$ [cm]	γ [deg.]	$\hat{\gamma}$ [deg.]	α [deg.]	$\hat{\alpha}$ [deg.]	β [deg.]	$\hat{\beta}$ [deg.]
23.81	24.07	27.24	28.51	-3.1	-1.21	-30	-28.21	0	-3.46	0	0.26
18.12	18.07	32.25	33.26	-3.1	-1.19	-20	-18.52	0	-2.98	0	-0.26
11.26	10.80	35.07	35.90	-4.1	-2.9	-10	-8.33	0	-2.46	0	-0.96
3	2.42	33.50	33.990	-4.1	-3.13	0	1.67	0	-1.55	0	-1.22
-2	-2	34.50	34.50	0.9	0.9	0	0	0	0	0	0
-11.26	-11.46	35.08	34.85	0.9	0.19	10	9.80	0	1.13	0	0.32
-20.94	-21.66	31.22	30.49	0.9	0.68	20	20.43	0	2.41	0	0.35
-25.54	-26.19	26.24	25.25	0.9	0.78	30	30.38	0	2.60	0	-0.02

(a) (b)

Fig. 10. Imaging of mannequin with attached scissors: a) without clothing; b) with clothing.

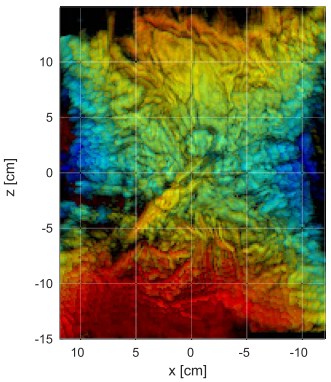

Fig. 11. Imaging of the scissors attached to mannequin after seven different scan positions using depth camera positioning.

Evaluation of the reflectivity at each position requires a computational time ranging from 1.05 s to 1.15 s that are in line with the times reported from the previous example. Again, a very good agreement with the real scene is found and the scissors, including the blade and the handles, can be seen in Fig. 11. The overlay of both models is also shown in Fig. 12.

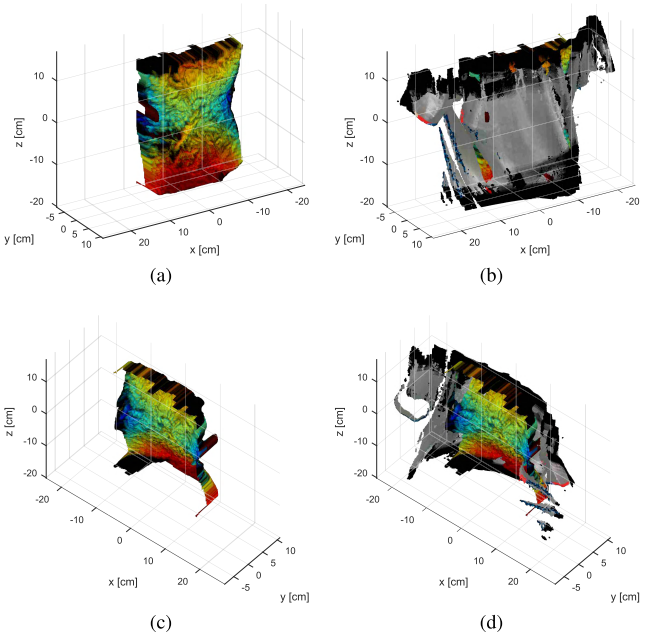

(a) (b) (c) (d)

Fig. 12. Imaging of a mannequin with attached scissors: a) front view of the mm-wave model; b) front view of the mm-wave model with the integrated PC; c) rear view of the mm-wave model; d) rear view of the mm-wave model with the integrated PC.

IV. CONCLUSIONS

In this paper, a multiview mm-wave scanner with positioning based on a depth camera has been analyzed. This arrangement bypasses the limitations of our previous setup [17], which required textured objects to find a number of key points from each view so that the position could be found by triangulation. On the contrary, the used depth camera positioning relies on comparing two consecutive point clouds and, therefore, it does not depend on textures. However, color information is still available and it could be applied for different purposes such as segmentation or by taking advantage of it during the ICP run [35]–[39].

In addition, the depth camera provides also a number of advantages, which are not available with a conventional camera. In particular, it is straightforward to set a clipping box

so that only the points inside a given cuboid are considered. Thus, the clutter due to external objects can be filtered out.

The results of the proof of concept reveal that the system requires a time ranging from approximately one to two seconds to update the model after acquiring the mm-wave and depth data. Therefore, it provides a reasonable responsive system, which could be moved into a real-time system by resorting to higher computational resources.

The obtained results show a very good fidelity with respect to the real-world scenario. It is also relevant to observe that, although the absolute error may reach 1.7 cm for a path of 73.7 cm, the relative error between two consecutive positions is in the order of a few millimeters. Consequently, although there could be inconsistencies between the opposite ends of the global model, no strange artifacts are observed locally and, therefore, the image information (e.g., whether there is a concealed weapon or not) can be easily inferred.

REFERENCES

[1] G. F. Marshall and G. E. Stutz, *Handbook of Optical and Laser Scanning*. Boca Raton, FL, USA: CRC Press, 2004.

[2] G. Guidi, J.-A. Beraldin, and C. Atzeni, "High-accuracy 3D modeling of cultural heritage: The digitizing of Donatello's 'Maddalena,'" *IEEE Trans. Image Process.*, vol. 13, no. 3, pp. 370–380, Mar. 2004.

[3] M. J. Westoby, J. Brasington, N. F. Glasser, M. J. Hambrey, and J. M. Reynolds, "'Structure-from-motion' photogrammetry: A low-cost, effective tool for geoscience applications," *Geomorphology*, vol. 179, pp. 300–314, Dec. 2012.

[4] P. Tanskanen, K. Kolev, L. Meier, F. Camposeco, O. Saurer, and M. Pollefeys, "Live metric 3D reconstruction on mobile phones," in *Proc. Int. Conf. Comput. Vis. (ICCV)*, Sidney, NSW, Australia, Dec. 2013, pp. 65–72.

[5] N. K. Nikolova, "Microwave imaging for breast cancer," *IEEE Microw. Mag.*, vol. 12, no. 7, pp. 78–94, Dec. 2011.

[6] A. T. Mobashsher, A. Mahmoud, and A. M. Abbosh, "Portable wideband microwave imaging system for intracranial hemorrhage detection using improved back-projection algorithm with model of effective head permittivity," *Sci. Rep.*, vol. 6, Feb. 2016, Art. no. 20459.

[7] D. M. Sheen, D. L. McMakin, and T. E. Hall, "Three-dimensional millimeter-wave imaging for concealed weapon detection," *IEEE Trans. Microw. Theory Techn.*, vol. 49, no. 9, pp. 1581–1592, Sep. 2001.

[8] S. Kharkovsky, J. T. Case, M. A. Abou-Khousa, R. Zoughi, and F. L. Hepburn, "Millimeter-wave detection of localized anomalies in the space shuttle external fuel tank insulating foam," *IEEE Trans. Instrum. Meas.*, vol. 55, no. 4, pp. 1250–1257, Aug. 2006.

[9] S. S. Ahmed, A. Schiessl, and L.-P. Schmidt, "A novel fully electronic active real-time imager based on a planar multistatic sparse array," *IEEE Trans. Microw. Theory Techn.*, vol. 59, no. 12, pp. 3567–3576, Dec. 2011.

[10] X. Zhuge and A. G. Yarovoy, "Three-dimensional near-field MIMO array imaging using range migration techniques," *IEEE Trans. Image Process.*, vol. 21, no. 6, pp. 3026–3033, Jun. 2012.

[11] H. Knapp *et al.*, "SiGe circuits for automotive radar," in *Proc. Top. Meeting Silicon Monolithic Integr. Circuits RF Syst.*, Jan. 2007, pp. 231–236.

[12] N. Dolatsha *et al.*, "A compact 130 GHz fully packaged point-to-point wireless system with 3D-printed 26 dBi lens antenna achieving 12.5 Gb/s at 1.55 pJ/b/m," in *IEEE Int. Solid-State Circuits Conf. (ISSCC) Dig. Tech. Papers*, Feb. 2017, pp. 306–307.

[13] A. Bisognin *et al.*, "Millimeter-wave antenna-in-package solutions for WiGig and backhaul applications," in *Proc. Int. Workshop Antenna Technol. (iWAT)*, Mar. 2015, pp. 52–55.

[14] A. Bisognin *et al.*, "Ball grid array-module with integrated shaped lens for WiGig applications in eyewear devices," *IEEE Trans. Antennas Propag.*, vol. 64, no. 3, pp. 872–882, Mar. 2016.

[15] M. T. Ghasr, M. A. Abou-Khousa, S. Kharkovsky, R. Zoughi, and D. Pommerenke, "Portable real-time microwave camera at 24 GHz," *IEEE Trans. Antennas Propag.*, vol. 60, no. 2, pp. 1114–1125, Feb. 2012.

[16] M. T. Ghasr, M. J. Horst, M. R. Dvorsky, and R. Zoughi, "Wideband microwave camera for real-time 3-D imaging," *IEEE Trans. Antennas Propag.*, vol. 65, no. 1, pp. 258–268, Jan. 2017.

[17] J. Laviada, A. Arboleya, Y. Álvarez, B. González-Valdés, and F. Las-Heras, "Multiview three-dimensional reconstruction by millimetre-wave portable camera," *Sci. Rep.*, vol. 7, Jul. 2017, Art. no. 6479, doi: 10.1038/s41598-017-06475-7.

[18] C. Wu, "Towards linear-time incremental structure from motion," in *Proc. Int. Conf. 3DTV*, Seattle, WA, USA, Jun. 2013, pp. 127–134.

[19] J. Laviada, A. Arboleya-Arboleya, and F. Las-Heras, "Multistatic millimeter-wave imaging by multiview portable camera," *IEEE Access*, vol. 5, pp. 19259–19268, 2017.

[20] P. Henry, M. Krainin, E. Herbst, X. Ren, and D. Fox, "RGB-D mapping: Using depth cameras for dense 3D modeling of indoor environments," in *Proc. Int. Symp. Experim. Robot. (ISER)*, Delhi, India, Dec. 2010, pp. 1–2.

[21] K. Khoshelham and S. O. Elberink, "Accuracy and resolution of Kinect depth data for indoor mapping applications," *Sensors*, vol. 12, no. 2, pp. 1437–1454, Feb. 2012.

[22] R. A. Morano, C. Ozturk, R. Conn, S. Dubin, S. Zietz, and J. Nissano, "Structured light using pseudorandom codes," *IEEE Trans. Pattern Anal. Mach. Intell.*, vol. 20, no. 3, pp. 322–327, Mar. 1998.

[23] S. Schuon, C. Theobalt, J. Davis, and S. Thrun, "High-quality scanning using time-of-flight depth superresolution," in *Proc. IEEE Comput. Soc. Conf. Comput. Vis. Pattern Recognit. Workshops*, Jun. 2008, pp. 1–7.

[24] J. N. Gollub *et al.*, "Large metasurface aperture for millimeter wave computational imaging at the human-scale," *Sci. Rep.*, vol. 7, Feb. 2017, Art. no. 42650.

[25] J. M. Lopez-Sanchez and J. Fortuny-Guasch, "3-D radar imaging using range migration techniques," *IEEE Trans. Antennas Propag.*, vol. 48, no. 5, pp. 728–737, May 2000.

[26] P. J. Besl and D. N. McKay, "A method for registration of 3-D shapes," *IEEE Trans. Pattern Anal. Mach. Intell.*, vol. 14, no. 2, pp. 239–256, Feb. 1992.

[27] R. B. Rusu and S. Cousins, "3D is here: Point cloud library (PCL)," in *Proc. IEEE Int. Conf. Robot. Autom. (ICRA)*, Shanghai, China, May 2011, pp. 1–4.

[28] K. Pulli, "Multiview registration for large data sets," in *Proc. 2nd Int. Conf. 3-D Digit. Imag. Modeling*, 1999, pp. 160–168.

[29] R. Toldo, A. Beinat, and F. Crosilla, "Global registration of multiple point clouds embedding the Generalized Procrustes Analysis into an ICP framework," in *Proc. 5th Int. Symp. 3D Data Process., Vis. Transmiss. (3DPVT)*, Paris, France, May 2010, pp. 109–122.

[30] A. Torsello, E. Rodolà, and A. Albarelli, "Multiview registration via graph diffusion of dual quaternions," in *Proc. CVPR*, Jun. 2011, pp. 2441–2448.

[31] J. Laviada, Y. Álvarez, A. Arboleya, F. Las-Heras, and B. G. Valdés, "Multiview techniques for mm-wave imaging," in *Proc. Antennas Propag. Symp. AP-S*, San Diego, CA, USA, Jul. 2017, pp. 1507–1508.

[32] G. Charvat, A. Temme, M. Feigin, and R. Raskar, "Time-of-flight microwave camera," *Sci. Rep.*, vol. 5, Oct. 2015, Art. no. 14709.

[33] A. Arboleya, Y. Álvarez, and F. Las-Heras, "Millimeter and submillimeter planar measurement setup," in *Proc. IEEE Antennas Propag. Soc. Int. Symp. (APSURSI)*, Jul. 2013, pp. 1–2.

[34] C. Wu. (2011). *VisualSFM: A Visual Structure From Motion System*. [Online]. Available: http://ccwu.me/vsfm/

[35] A. E. Johnson and S. B. Kang, "Registration and integration of textured 3-D data," in *Proc. Int. Conf. Recent Adv. 3-D Digit. Imag. Modeling*, May 1997, pp. 234–241.

[36] S. Druon, M.-J. Aldon, and A. Crosnier, "Color constrained ICP for registration of large unstructured 3D color data sets," in *Proc. IEEE Int. Conf. Inf. Acquisition*, Aug. 2006, pp. 249–255.

[37] L. Douadi, M. J. Aldon, and A. Crosnier, "Pair-wise registration of 3D/color data sets with ICP," in *Proc. IEEE/RSJ Int. Conf. Intell. Robots Syst.*, Oct. 2006, pp. 663–668.

[38] J. Gómez-García-Bermejo, E. Zalama, and R. Feliz, "Automated registration of 3D scans using geometric features and normalized color data," *Comput.-Aided Civil Infrastruct. Eng.*, vol. 28, no. 2, pp. 98–111, 2013.

[39] M. Korn, M. Holzkothen, and J. Pauli, "Color supported generalized-ICP," in *Proc. Int. Conf. Comput. Vis. Theory Appl. (VISAPP)*, vol. 3. Jan. 2014, pp. 592–599.

JAIME LAVIADA was born in Gijón, Spain. He received the M.S. degree in telecommunication engineering and the Ph.D. degree from the Universidad de Oviedo, Spain, in 2005 and 2010, respectively. In 2006, he joined the research group Signal Theory and Communications, Universidad de Oviedo, where he has been involved in multiple national and European projects as well as contracts with several companies. He was a Visiting Scholar with the Electromagnetics and Communications Lab, Pennsylvania State University, from 2007 to 2008. In 2015, he was with the Antennas Group, Universidad Pública de Navarra, with a National Post-Doctoral Fellowship collaborating in several applied research projects. He was with the Universidad de Oviedo, where he is currently an Assistant Professor. He was a Visiting Scholar with the Applied Microwave NonDestructive Testing Laboratory, Missouri S&T, in 2017. He currently serves as an Associated Editor for the IEEE Access.

His research interests include numerical techniques applied to electromagnetic imaging, antenna measurements, method of moments, and antenna pattern synthesis.

MIGUEL LÓPEZ-PORTUGUÉS received the degree in computer science and the Ph.D. degree from the University of Oviedo, Spain, in 2008 and 2017, respectively. He is currently a Research Assistant with the TSC-UNIOVI Group, University of Oviedo. His main research interests include parallel and high-performance computing, computer vision, and fast iterative methods applied to electromagnetic and acoustic scattering problems.

ANA ARBOLEYA-ARBOLEYA received the M.Sc. degree in telecommunication engineering in 2009 and the Ph.D. degree in telecommunication engineering from the University of Oviedo, Spain, in 2016. From 2008 to 2016, she was a Research Assistant with the Signal Theory and Communications Research Group (TSC-UNIOVI), Department of Electrical Engineering, University of Oviedo. She was a Visiting Scholar with the MilliLab, Department of Radio Science and Engineering, Aalto University, Finland, in 2014 and 2015. She held a post-doctoral position at the EpOC Polytech' Lab (Electronics for Connected Objects), University of Nice-Sophia Antipolis, France, in 2017. She is currently an Assistant Professor with Universidad Rey Juan Carlos, Madrid, Spain.

Her major research interests include antenna diagnostics and measurement systems and techniques, and high frequency imaging techniques and applications. He was a recipient of the 2017 National Awards of the Official College of Telecommunication Engineers of Spain to the best Ph.D. thesis on Telecommunication Engineering in the category of security and defense.

FERNANDO LAS-HERAS (M'86–SM'08) received the M.S. and Ph.D. degrees in telecommunication engineering from the Technical University of Madrid (UPM), in 1987 and 1990, respectively. He was a National Graduate Research Fellow from 1988 to 1990 and he was an Associate Professor with the Department of Signal, Systems and Radiocommunications, UPM, from 1991 to 2000. He was a Visiting Lecturer with the National University of Engineering, Peru, in 1996, and a Visiting Researcher with Syracuse University, Syracuse, NY, USA, in 2000. Since 2001, he has been the Head of the Research Group Signal Theory and Communications TSC-UNIOVI, Department of Electrical Engineering, University of Oviedo. Since 2003, he has been a Full Professor with the University of Oviedo, where he was the Vice-Dean of the telecommunication engineering with the Technical School of Engineering at Gijón, from 2004 to 2008. He was a short term Visiting Lecturer with ESIGELEC, France, from 2005 to 2011. He held the Telefónica Chair on RF Technologies, ICTs applied to Environment and ICTs and Smartcities with the University of Oviedo from 2005 to 2015. He is a member of the board of directors of the IEEE Spain Section from 2012 to 2015, the board the IEEE Microwaves & Antennas Propagation Chapter (AP03/MTT17) from 2016 to 2017, the Science, Technology and Innovation Council of Asturias in 2010, and the President of the professional association of Telecommunication Engineers, Asturias. He has led and participated in a great number of research projects and has authored over 190 technical journal papers, mainly in the areas of antennas, propagation, metamaterials and inverse problems with application to antenna measurement (NF-FF, diagnostics, and holography), electromagnetic imaging (security and NDT), and localization, developing computational electromagnetics algorithms and technology on microwaves, millimeter wave, and THz frequency bands.